Available online at website: https://jurnal.iaii.or.id/index.php/RESTI

JURNAL RESTI

(Rekayasa Sistem dan Teknologi Informasi)

Vol. 9 No. 3 (2025) 477 - 486 e-ISSN: 2580-0760

Classification of Retinoblastoma Eye Disease on Digital Fundus Images Using Geometric Features and Machine Learning

Arif Setiawan

Department of Information System, Faculty of Engineering, Muria Kudus University, Kudus, Indonesia

arif.setiawan@umk.ac.id

Abstract

Medical image analysis is essential for detecting retinoblastoma tumors due to the ability of this method to assist doctors in examining the morphology, density, and distribution of blood vessels. The classification of normal and retinoblastoma-affected retinas is a preliminary step in treating retinoblastoma tumors. Therefore, this study aimed to propose a new method for classifying normal and retinoblastoma-affected retinas using geometric feature extraction and machine learning. The workflow consisted of (1) fundus image data collection for retinoblastomas, (2) image segmentation, (3) feature extraction process, (4) building a classification model using machine learning, (5) splitting testing and training data, (6) classification process using machine learning methods, and (7) evaluation of classification results using a confusion matrix. The results showed that the segmentation method could detect retinoblastoma areas and extract their geometric features. The SVM method achieved an accuracy of 0.96 while the RF and DT had 0.55 and 0.63, respectively. Moreover, a comparison with previous research showed that the proposed method achieved a 4% improvement in the classification performance. This led to the conclusion that classification using geometric features combined with the SVM on digital fundus images of retinoblastoma eye disease produced the best results.

***Keywords**:* retinoblastoma; digital fundus images; classification; geometric features; machine learning

How to Cite: A. Setiawan, "Classification of Retinoblastoma Eye Disease on Digital Fundus Images Using Geometric Features and Machine Learning", *J. RESTI (Rekayasa Sist. Teknol. Inf.)* , vol. 9, no. 3, pp. 477 - 486, May 2025.
*Permalink/*DOI: https://doi.org/10.29207/resti.v9i3.6337

Received: January 29, 2025
Accepted: May 4, 2025
Available Online: May 24, 2025

This is an open-access article under the CC BY 4.0 License
Published by Ikatan Ahli Informatika Indonesia

1. Introduction

The introduction section sets the stage for your study by providing context, defining the problem, highlighting its significance, and outlining your contribution. It should engage the reader, establish the relevance of your work, and clearly articulate the objectives of the research.

Retinoblastoma is an eye cancer that invades the retinal cells, damages eye tissue, and leads to blindness. It is a solid tumor characterized by the appearance of strabismus and leukocoria [1]. The treatment includes intra-arterial chemotherapy (IAC) which is capable of curing retinoblastoma with a success rate of up to 88.2% and reducing the metastasis process to 1.6% based on analyses [2]. The tumor leads to bleeding in the posterior ciliary artery of the outer retina and grows aggressively in vascular tissues [3]. An important observation is that retinoblastoma is an intraocular and malignant tumor commonly found in children under the age of eight. The average age of diagnosis is between two and five years. Moreover, it is often clinically diagnosed with the assistance of B-scan ultrasound (USG B-scan) [4].

Patients experience targeted intra-arterial therapy, supplemented with radiotherapy to inhibit tumor growth and preserve the eyeball. However, some patients experience retinal detachment after the surgery due to the medication and surgical remnants [5]. This shows the importance of medical image analysis for detecting retinoblastoma tumors. The method aids doctors in examining the morphology, density, and distribution of blood vessels as well as assessing pathology and performing accurate diagnostic evaluations [6]. Different image analysis methods have been applied in the healthcare field, particularly for retinal examinations, with a focus on diseases such as retinal detachment, diabetic retinopathy, glaucoma, and retinoblastoma [7]. Medical images are acquired through imaging methods and are used to diagnose different types of diseases. These images serve as inputs for Artificial Intelligence (AI) systems and provide the quantitative data required by AI models [8].

This research preferred geometric features as the primary method for the classification of retinoblastoma eye disease due to their advantages in terms of efficiency, interpretability, and the limitations of implementing deep learning methods in medical contexts. Moreover, geometric features such as the width, height, and area of abnormal regions are easily understood by medical professionals. These are different from the abstract features produced by convolutional neural networks (CNNs), which are difficult to interpret directly. Geometric features have clear visual and clinical representations which assist physicians to comprehend the rationale behind the decisions made through the classification system. The trend is in line with the principles of explainable Artificial Intelligence (XAI) in the medical field.

Machine learning methods associated with geometric features are also computationally more efficient compared to CNNs which require significant computational resources, GPU support, and longer training times. Therefore, these methods can be implemented on low-specification systems or used in real-time within clinical environments with hardware limitations. Deep learning methods, particularly CNNs, generally require large volumes of training data to produce accurate and generalized models. Meanwhile, there were limited digital fundus image datasets for retinoblastoma cases in this research and the geometric feature-based method provided a more appropriate and robust solution for small-scale datasets.

Smith explained the use of Doppler imaging to measure the volume of retinoblastoma tumors. The research utilized 20 images from retinoblastoma patients and Doppler imaging was adopted to predict the response of retinoblastoma to IAC. It was concluded that retinoblastoma tumor volume correlated with Doppler features from the Central Retinal Artery (CRA) [2]. Ramasubramanian also described the use of microvascular flow imaging (MFI) to identify the vascular characteristics of retinoblastoma tumors. The research used data from the eyes of 10 patients and MFI showed branching patterns of blood vessels in all examined eyes [3]. Furthermore, Xiao utilized U-net segmentation to analyze fundus images using 125 retinal fundus images and the texture features adopted produced an accuracy of 93.7% [9].

Huang developed the Dual Guidance Module (DGM) and Refinement Guidance Module (RGM) for analyzing retinal fundus image data. DGM was used to extract vascular frameworks and segment blood vessels using image enhancement methods while RGM was adopted to produce more accurate results [10]. Fang also applied Gabor-net and a combination of multi-scale hierarchical features to analyze retinal fundus data. Blood vessel information was obtained using the main channel of the Residual Block convolution and combined with the Retina-Exogenous-Primary Visual Cortex. Gabor-net was used to simulate the main pathway of the convolutional network and the process led to the production of more precise blood vessel information [11]. Moreover, Huang utilized deep learning to analyze retinal digital fundus images. The focus was on 467 eyes from 463 patients and the application of deep-learning CNN methods, including ResNet50, VGG19, and InceptionV3. The variables considered were the image quality, eye, location, phase, lesion, diagnosis, and macular participation. The research achieved an accuracy ranging from 81.72% to 96.45% [12]. Another research by Xia used a large dataset comprising 28,877 retinal digital fundus images which were analyzed by applying a Transformer-joint convolution network for automated eye disease screening. The diseases analyzed include diabetic retinopathy, age-related macular degeneration, glaucoma, pathological myopia, hypertension retinopathy, retinal vein occlusion, and laser photocoagulation [13].

Wong developed a machine learning model for multi-class classification of diabetic retinopathy, central retinal vein occlusion, and branch retinal vein occlusion using fundus color photographs. The research utilized 3,200 digital fundus images and achieved an accuracy of 97.5% [14]. Moreover, Liu reconstructed spectral fundus images using a Retinex Transformer-based semantic model. The multispectral imaging is a non-invasive method for measuring retinal oxygen saturation levels. This proposed model utilized RGB images to reconstruct multispectral images which enabled an improvement in retinal oximetry and diagnostic capabilities [15]. Another research by Balasubramaniam used CNN transfer learning to detect the optic disc and predict cardiovascular risks from retinal digital fundus images. The detection method was an active counter model called Osprey Gannet which was designed and trained with Osprey Gannet optimization, leading to an accuracy of 92.1% [16]. Furthermore, Nuli addressed the semantic segmentation problem for data on retinal digital fundus images. The research examined the effectiveness of data augmentation using Gamma-corrected images and the application of the U-Net segmentation method led to an improvement in the Gamma correction performance, with the optimal Gamma value recorded to be 0.75 [8]. This study is important because retinoblastoma is a serious disease that requires early detection and treatment to prevent vision loss and the risk of death. The objects were digital fundus images of the eyes that contained visual information regarding the condition of the retina. The specific focus is on cases of retinoblastoma, which is a type of eye cancer affecting the retina and commonly occurs in children. Previous research has focused on detecting and classifying retinoblastoma eye disease, but most studies have focused on diabetic retinopathy

Geometric features were not utilized in the extraction process of the digital fundus images. Consequently, this study aimed to obtain the geometric features of digital fundus images of retinoblastoma, detect the cancerous area, and classify normal and affected eyes. This was essential to ensure that the developed method could detect retinoblastoma more swiftly and accurately, facilitating earlier and more precise medical interventions. This method enables the automatic identification and classification of retinoblastoma, thereby reducing the subjectivity inherent in human visual evaluations. Additionally, it has the potential to serve as a foundation for further research on classifying other eye diseases or developing intelligent diagnostic systems based on medical imaging. This trend indicates that this research contributes to the development of a new method for classifying normal retina and retinoblastoma eye diseases using geometric features and machine learning, marking an initial step in the treatment of retinoblastoma tumors.

2. Methods

Image segmentation was used to extract features by dividing digital images into smaller segments to enable complete analysis of the information [17]. This process is necessary because reading digital images poses challenges, such as uneven lighting, excessive noise, and inconsistent brightness levels [18]. Therefore, image segmentation is often used to separate objects in an image from the background [19]. It was applied in this research to convert color images into grayscale images consisting of pixel values ranging from 0 to 255, where 0 represented black and 255 was white [17]. Grayscale values represent brightness intensity levels [20] which subsequently function as detectors in image processing to assist in distinguishing the background from the foreground. These values were calculated using Equation 1 [21].

$$x = 0{,}299r + 0{,}587g + 0{,}114b \tag{1}$$

The next process was to convert the grayscale images into binary images with pixel values of 0 and 1 [22]. Binary images were used to separate the object from the background using thresholding [23]. The method divided pixel values into two categories, including the foreground and background. The formula used for the conversion of grayscale images into binary images is presented as Equation 2 [24].

$$g(x,y) = \begin{Bmatrix} 1, if\ f(x,y) \geq T \\ 1, if\ f(x,y) \geq T \end{Bmatrix} \tag{2}$$

Part of the methods most commonly used for the conversion is the Otsu. This method identifies the threshold point that distinguishes black from white [25] and determines different classes with the largest variance [24]. The calculation for the threshold value was based on Equations 3 and 4.

$$L = [1,2,3, \dots L] \tag{3}$$

$$N = n1 + n2 + n3 + \cdots + nl \tag{4}$$

The pixel values of the two sections became classes, background *Cb* and foreground *Cf*. This was achieved through the provision of a threshold value t:

$$Cb = [1,2,3, \dots t] \tag{5}$$

$$C_f = [t+1, t+2, t+3, \dots L] \tag{6}$$

The formula used to determine the background and foreground variance for the t threshold value is presented as Equations 7 through 12:

Background Cb:

$$\text{Weight } W_b = \sum_{i=1}^{t} \frac{n_i}{N} \tag{7}$$

$$\text{Average } \mu_b = \frac{\sum_{i=1}^{t} i * n_i}{\sum_{i=1}^{t} n_i} \tag{8}$$

$$\text{Varian } \sigma_b^2 = \frac{\sum_{i=1}^{t} (i-\mu_b)^2 * n_i}{\sum_{i=1}^{t} n_i} \tag{9}$$

Foreground Cf:

$$\text{Weight } W_f = \sum_{i=1+1}^{L} \frac{n_i}{N} \tag{10}$$

$$\text{Average } \mu_b = \frac{\sum_{i=1}^{L} i * n_i}{\sum_{i=1}^{L} n_i} \tag{11}$$

$$\text{Varian } \sigma_f^2 = \frac{\sum_{i=1+1}^{L} (i-\mu_f)^2 * n_i}{\sum_{i=1+1}^{L} n_i} \tag{12}$$

The variance in class σ_w^2 is the sum of the two variances multiplied by the weight. This is presented in Equation 13:

$$\sigma_w^2 = W_b \sigma_b^2 + W_f \sigma_f^2 \tag{13}$$

Geometric features often used in image analysis are calculated as the distance between two points in an image [26]. Therefore, Euclidean distance was used to measure the distance between two pixels in an image and the value was converted into centimeters or millimeters [27]. Geometric recognition was also used to reconstruct the two-dimensional geometry of an image. This is possible because images can be based on their geometry, including small and large sections. This geometry can be two-dimensional (2D) or three-dimensional (3D), depending on the segmentation process requirements [28]. Some of the geometry feature methods include Random Sample Consensus (RANSAC) which utilizes geometric coordinates to eliminate outliers as well as Graph Transformation Matching (GTM), Restricted Spatial Order Constraints (RSOC), and Triangle Area Representation of the K Nearest Neighbors (KNN-TAR) [29].

Table 1. Geometric Features of Retinoblastoma

Features	Symbol
Width	W
Height	H
Wide Area	A

Vertical and horizontal lines were extracted through the geometric features to determine object sizes within an image. Moreover, angle measurements can be performed using trigonometric formulas. The results for both the lines and angles are often stored in a database for further processing using machine and deep learning methods [30]. The geometric features of the retinoblastoma digital fundus images used in this research are presented in Table 1.

The Euclidean distance is an extension of the Pythagorean theorem (Bourdeau dkk., 2021) and is considered applicable to both 2D and 3D objects. For 2D objects, its application is typically used in digital images specifically to calculate the distance between the initial (x,y) and the final coordinates (x',y') (Gandla dkk., 2020). The Euclidean distance was applied through Equation 14 (Andries dkk., 2020):

$$d(a,b) = \sqrt{(x' - x)^2 + (y' - y)^2} \quad (14)$$

The method is part of the matrix distance measures often used to evaluate the similarity and proximity between two data points. A smaller Euclidean distance between two image matrices shows higher similarity and the degree can be measured using features of digital images, such as color, texture, shape, and size [34].

Machine learning is a branch of AI that consists of three main methods of processing data, including supervised, unsupervised, and deep [35]. Supervised learning identifies patterns in input data and their corresponding output labels. Machine learning models are trained to recognize input data that is correlated with predefined outputs. Therefore, the purpose of supervised learning is to produce output based on prior experience [36]. This method has two types of variables which include input and output. Moreover, some examples of supervised learning include classification and regression [37] which are widely used for prediction and classification tasks. Some common machine learning methods include Support Vector Machine (SVM), Random Forest (RF), and Decision Tree (DT) [38].

Support Vector Machine (SVM) is a supervised learning method for regression and classification. In the classification process, it is used to separate objects into multiple classes using linear, polynomial, and Radial Basis Function (RBF) kernels [39]. SVM is used to process large and high-dimensional data, and the selection of appropriate parameters can significantly affect its performance [40]. This method aims to determine the optimal hyperplane that separates the classes. Furthermore, a hyperplane is a decision function positioned in the middle to divide the classes [41]. SVM can make accurate classification predictions by using support vectors for the hyperplane. These support vectors pass through the data points to determine the maximum margin [42].

SVM for regression aims to predict the output of new data using continuous output values. Meanwhile, the application of the method for classification focuses on classifying input data to produce class as the output [43]. SVM uses several kernels presented as Equations 15 through 17 to transform data:

Linear kernel

$$K(x_i, x) = x_i^T x \quad (15)$$

x_i is the training data and x is the test data.

Polynomial kernel

$$K(x_i, x) = (y(x_i^T x) + r)^p \quad (16)$$

Sigmoid kernel

$$K(x_i, x) = tanh(y(x_i^T x) + r) \quad (17)$$

Random Forest (RF) is a machine learning algorithm that consists of an ensemble of decision trees. It can also be used for regression and classification tasks on large datasets. The method operates by constructing decision trees to produce regression results (Gao dan Zhou, 2020). RF combines multiple trees during the training process and the number of trees used directly impacts the accuracy of the results. This is based on the condition that a greater number of trees leads to higher accuracy [45].

RF is a supervised learning algorithm that can address both classification and regression problems. Its distinctive feature is that each tree is grown on a bootstrap sample randomly drawn from the training data [46]. During each node split in the decision tree formation, a subset of mmm variables is randomly selected from the original dataset, and the best is used for the node. The prediction of RF consisting of NNN trees can be achieved using Equation 18:

$$l(y) = argmax_c(\sum_{n=1}^{n} I_{h_n(y)=c}) \quad (18)$$

I is an indicator function and h_n is the n-th tree in the RF.

Decision Tree (DT) is a machine learning algorithm used to create decision rules in a tree-like structure. It is also a supervised learning method applicable to both classification and regression tasks [47]. DT uses tree-structured rules to make decisions with branches representing decision paths to achieve optimal results [48]. The main components include the root node which is the main goal or output of the DT, branches represent different decision paths or actions, decision nodes are points where decisions are made based on the features of the input data, and leaf nodes are the outcomes or results of the decisions. This method starts with a single node, which branches out to represent available choices. The steps to build a DT include recursive development of the tree starting with the root node that contains all training examples. A test is conducted to decide the branching path. However, step 1 needs to be revisited when the correct branch is identified and a leaf node is not reached. Attributes are divided into categories and the selected node can be determined using the entropy value of each criterion based on the sample data provided. The selected node is the criterion with the smallest entropy value which is calculated using Equation 19.

$$Entropy\ (S) = \sum_{i=1}^{n} -pi * log_2\ pi \quad (19)$$

The test attribute is selected based on heuristics or statistical measures such as Information Gain, which measures the effectiveness in classifying the data. This Information Gain can be calculated using Equations 20 and 21.

$$Gain(S, A) = Entropy(S) - \sum_{i=1}^{n} \frac{|Si|}{|s|} * Entropy(si) \quad (20)$$

S is the set of cases, *n* is the number of partitions in *S*, and *pi* is the proportion of *Si* relative to *S*.

$$Gain(S, A) = Entropy(S) - \sum_{i=1}^{n} \frac{|Si|}{|s|} * Entropy(si) \quad (21)$$

S is the set of cases, *A* is the attribute, *n* is the number of partitions of attribute *a*, $|Si|$ is the number of cases in partition *i*, and $|s|$ is the total number of cases in *S*.

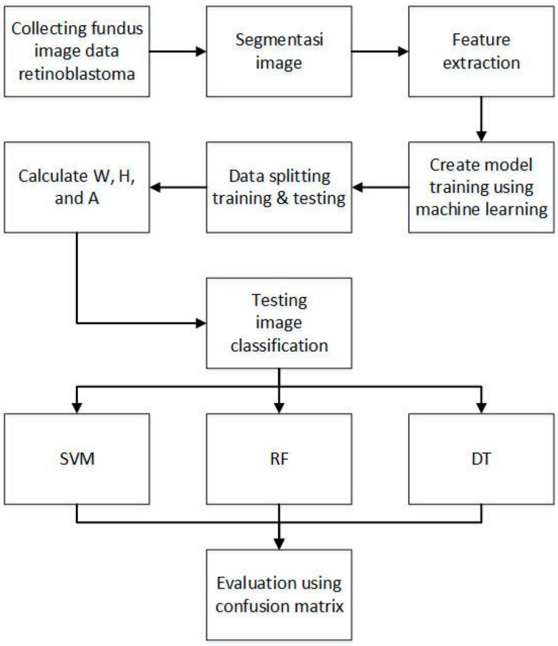

Figure 1. Research Steps

The steps used to conduct this research include (1) collection of digital fundus images related to retinoblastoma from the American Society of Retina Specialists (ASRS) retina image bank in the form of RGB images in JPEG format. The next was the (2) segmentation process which was used to convert the images from color to grayscale and subsequently binary followed by edge detection using the Canny method. (3) The feature extraction step was focused on detecting the edge coordinates through the blob detection method, identifying blob points, and measuring distances between edge points. Moreover, the Euclidean Distance method was applied to determine the width, height, and area of the retinoblastoma region. The next step was to (4) develop a classification model using machine learning methods, including SVM, RF, and DT. This was followed by (5) splitting the data into training and testing sets using the K-Fold Cross Validation method. Furthermore, (6) the classification process was conducted using machine learning methods through 72 images used as training data and 46 images as testing data. The last step was to (7) evaluate classification results using a confusion matrix with a focus on accuracy, precision, recall, and F1-score. These stages are presented comprehensively in Figure 1.

3. Results and Discussion

This research aims to classify between normal retina and retinoblastoma using data obtained from a retinal image bank. Retinoblastoma detection was conducted using a segmentation method through different machine learning such as SVM, RF, and DT [49]. The research was initiated by collecting 120 data on retinal fundus images which were categorized into two classes, including normal retina and retinoblastoma. The dataset was further divided into two parts, including 74 for training and 46 for testing. The data were obtained from the Retina Image Bank of the ASRS and data augmentation methods were not applied to the processing. The next step was the segmentation process to convert the digital fundus images of retinoblastoma into grayscale format [50]. This step was used to detect the retinoblastoma area as presented in Figure 2.

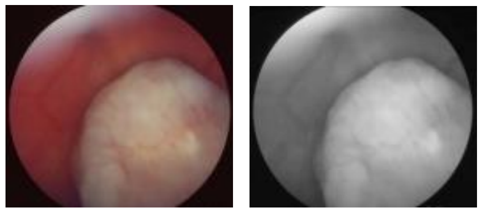

(a) (b)
Retinoblastoma 1

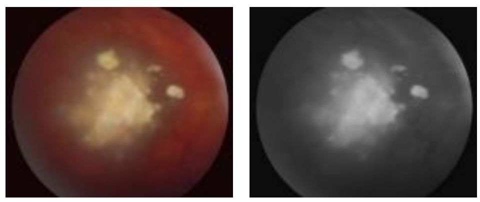

(a) (b)
Retinoblastoma 2

(a) (b)
Retinoblastoma 3

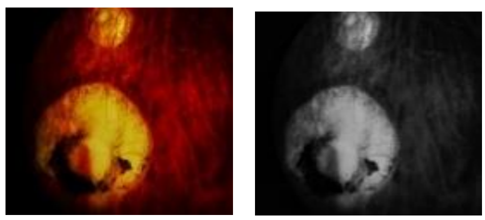

(a) (b)
Retinoblastoma 4

Figure 2. (a) Colored Digital Retinoblastoma Image Fundus, (b) Grayscale Image

The grayscale images were further converted into binary format. The purpose was to separate the retinoblastoma area from the background.

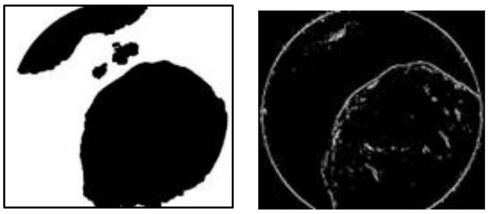

(a) (b)
Retinoblastoma 1

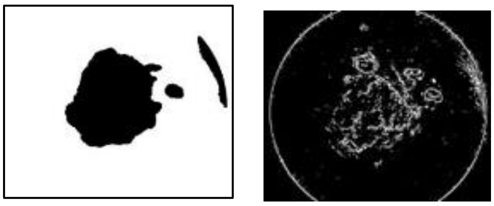

(a) (b)
Retinoblastoma 2

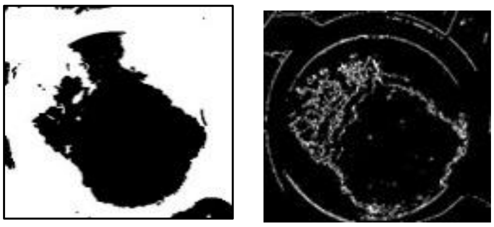

(a) (b)
Retinoblastoma 3

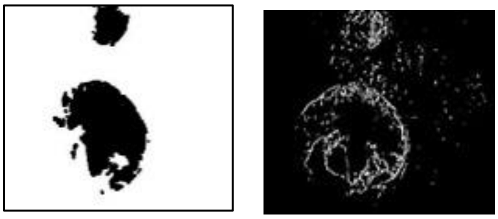

(a) (b)
Retinoblastoma 4

Figure 3. (a) Binary Image, (b) Edge Detection

The conversion process was conducted through the application of the Otsu method [24]. The next process was edge detection, which was used to identify the boundary of the retinoblastoma area in the binary images through the application of the Canny method [51]. The detailed results of the binary image and edge detection are shown in Figure 3.

The research proceeded with the detection of the edge coordinates. This was achieved by using the length, width, and area to detect the geometric features of the retinoblastoma region, which were selected as the primary attributes for the extraction process instead of texture and color. This preference was based on several technical and clinical considerations associated with the use of geometric features in the classification of retinoblastoma in digital fundus images. Some of these include the ability to provide clinically interpretable information, such as the size, shape, and spatial distribution of abnormal regions through the lesion area, width, height, and aspect ratio. Moreover, the features are directly related to anatomical structures that can be visually observed, which makes them easier for medical professionals to understand compared to the abstract statistical representations of texture or color.

The morphological characteristics of retinoblastoma serve as key indicators in clinical diagnosis. These characteristics typically exhibit distinct shapes and spatial patterns that can be effectively represented through geometric descriptors. Meanwhile, texture or color features often fail to clearly distinguish between normal and abnormal retinas. The extraction process of geometric features is also simpler and more computationally efficient, in line with the objective of developing a lightweight and easily deployable diagnostic system. This is different from texture features which generally require more complex computations such as Gray-Level Co-occurrence Matrix (GLCM) or Local Binary Pattern (LBP). Color features also have the capacity to increase data dimensionality which consequently raises computational load without necessarily improving model performance.

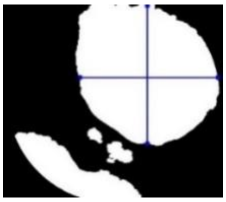

Width: 12.12 mm
Height: 10.66 mm
Wide Area: 129.21 mm^2

Retinoblastoma 1

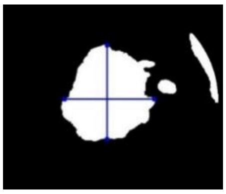

Width: 12.33 mm
Height: 10.37 mm
Wide Area: 127.88 mm^2

Retinoblastoma 2

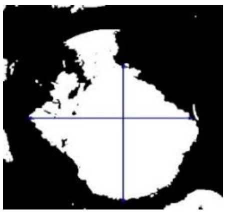

Width: 16.99 mm
Height: 15.80 mm
Wide Area: 268.31 mm^2

Retinoblastoma 3

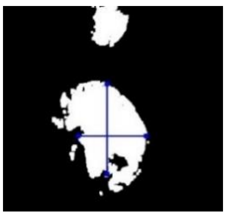

Width: 13.94 mm
Height: 10.48 mm
Wide Area: 146.09 mm^2

Retinoblastoma 4

Figure 4. Geometric Features, the Length, Width, and Wide Area of the Retinoblastoma

The coordinate points obtained from the edge detection process were connected by diagonal lines to represent the length and width. As previously stated, the distance between the two points was calculated using Euclidean Distance [32]. The length and width, measured in pixels, were converted to millimeters (mm) and applied to estimate the retinoblastoma area. The results of the coordinate detection are comprehensively presented in Figure 4 and the geometric features in Figure 5.

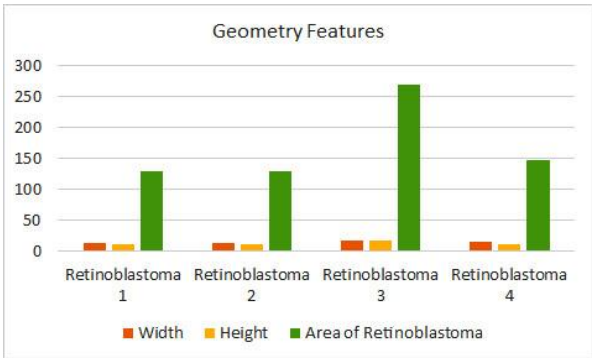

Figure 5. Geometric Features of Retinoblastoma

	precision	recall	f1-score	support
Retinoblastoma	0.98	0.87	0.93	74
Normal retina	0.87	0.98	0.95	46
accuracy			0.96	120
macro avg	0.97	0.95	0.96	120
weighted avg	0.97	0.96	0.96	120

SVM

	precision	recall	f1-score	support
Retinoblastoma	0.97	0.39	0.55	74
Normal retina	0.71	0.97	0.83	46
accuracy			0.75	120
macro avg	0.86	0.70	0.69	120
weighted avg	0.84	0.75	0.71	120

RF

	precision	recall	f1-score	support
Retinoblastoma	0.51	1.00	0.56	74
Normal retina	1.00	0.40	0.83	46
accuracy			0.63	120
macro avg	0.77	0.72	0.62	120
weighted avg	0.83	0.63	0.61	120

DT

Figure 6. Results of Confusion Matrix

The next step was the feature extraction process of retinal images from 120 data points for the two classes, including normal retina and retinoblastoma. The geometric features obtained were used to build a machine learning model [52]. Moreover, the data retrieved were split into two sets, including testing and training, using K-Fold Cross Validation followed by the application of the three machine learning methods, SVM, RF, and DT, to produce the confusion matrix presented in Figure 6. The results showed that SVM had the best performance, with a classification accuracy of 0.96, precision of 0.97, recall of 0.95, and F1-Score of 0.96. The precision was the ratio of True Positive (TP) to the total number of positive predictions while recall was the ratio of TP to the total number of actual positive cases. F1-Score is the harmonic average of precision and recall [53]. The achievement of a good F1-Score is the representation of effectiveness in both precision and recall. The detailed results of classification accuracy, precision, recall, and F1-Score for the three machine learning methods are presented in Figure 7.

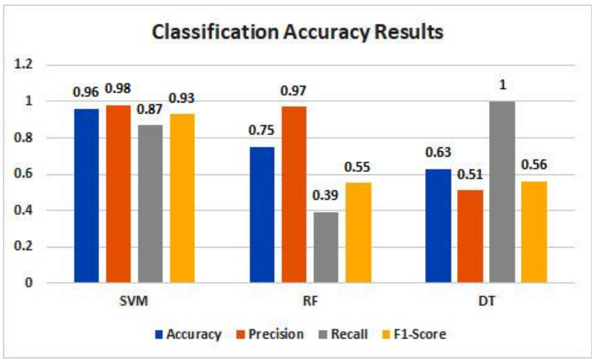

Figure 7. Classification Accuracy, Precision, Recall, and F1-Score

The basic explanation, relationship, and generalization of the results are the contents of the discussion. The purpose is to answer the research question and objectively identify any dubious result.

Table 2. Results of classification

Methods	Accuracy	Precision	Recall	F1-Score
SVM	0.96	0.98	0.87	0.93
RF	0.75	0.97	0.39	0.55
DT	0.63	0.51	1.00	0.56

The classification accuracy results are comprehensively explained in Table 2. Moreover, the results showed improved performance compared to previous research as presented in Table 3.

Table 3. Research comparison

Research	Methods	Classification Accuracy
[9]	Texture Features and U-Net Segmentation	0.93
[16].	CNN transfer learning	0.92
[12].	ResNet50, VGG19, InceptionV3	0.81-0.95
[8]	U-Net Segmentation	0.75
This research	Geometry features and SVM	0.96

The observed classification errors were primarily caused by the poor quality of some fundus images, such as uneven lighting conditions, which affected the geometric feature extraction process. Therefore, the extracted features did not accurately represent the actual structure of the retina, making it difficult to distinguish between normal and abnormal classes. The geometric features of retinoblastoma and normal retina images also exhibited similar values, particularly in those with less distinctive morphological characteristics, leading to a feature overlap between classes. Furthermore, the dataset used was limited in both quantity and diversity, which prevented the model from fully recognizing all possible variations in retinoblastoma patterns that are capable of appearing in real-world cases. The lack of representative data also contributed to the suboptimal generalization performance of the model. Potential bias occurred owing to the varying image contrast levels in the dataset, which caused the developed model to experience significant differences.

The machine learning models used were executed using default parameter settings without hyperparameter tuning or optimization. This allowed the classification performance to reflect the pure effectiveness of the selected features without being influenced by the tuning processes. Moreover, the use of default settings represents a more practical and easily replicable method, especially when the system is intended to be widely implemented in clinical environments with technical limitations. Models with standard configurations are also easier to deploy by medical personnel or technicians who do not have an extensive background in machine learning.

Expert judgment assessments were conducted in clinical trials by eye disease specialists. This was necessary to ensure that the geometric features extracted from fundus images truly represented the clinical characteristics of retinoblastoma. The evaluation also included the appropriateness of the feature extraction methods applied based on scientific standards and medical practice. Furthermore, the effectiveness of the SVM in handling small-to medium-sized datasets and its classification accuracy were assessed. The potential bias due to variations in image contrast across the dataset and its impact on model performance were also evaluated, along with the practical usability of the system and its contribution to the early detection of retinoblastoma.

4. Conclusions

In conclusion, this study used image geometry feature extraction and machine learning to classify normal retinas and retinoblastomas. The results showed that the length and width of the detected retinoblastoma area were the extractable geometric features. The machine-learning methods used were SVM, RF, and DT. Among the three algorithms, SVM achieved the highest classification accuracy, with a value of 0.96. This led to the conclusion that the development of geometric feature extraction methods and the SVM machine learning method produced the best results in classifying normal and retinoblastoma retinal images and contributed new insights in the field of eye health.

Future research should focus on expanding the classification to include different types of retinal diseases using digital fundus images and deep learning as well as the application of the XAI method with larger data.

Acknowledgments

The authors are grateful to the Department of Information Systems, Faculty of Engineering, Muria Kudus University, for supporting this research. The author declares no conflict of interest. Moreover, no specific grant was received from any funding agency in the public, commercial, or not-for-profit sectors.

References

[1] S. Wang, Y. Zhao, F. Yao, P. Wei, L. Ma, and S. Zhang, "An anti-GD2 aptamer-based bifunctional spherical nucleic acid nanoplatform for synergistic therapy targeting MDM2 for retinoblastoma," *Biomed. Pharmacother.*, vol. 174, no. March, p. 116437, 2024, doi: 10.1016/j.biopha.2024.116437.

[2] K. Mcinnis-smith, T. Abruzzo, M. Riemann, L. F. Goncalves, and A. Ramasubramanian, "Utility of color Doppler imaging in patients with retinoblastoma treated by intra-arterial chemotherapy," *J. AAPOS*, no. 3, p. 104093, doi: 10.1016/j.jaapos.2024.104093.

[3] A. Ramasubramanian, M. Riemann, A. Brown, T. Abruzzo, and L. F. Goncalves, "Microvascular flow ultrasound imaging for retinoblastoma," *J. AAPOS*, vol. 28, no. 1, p. 103801, 2024, doi: 10.1016/j.jaapos.2023.10.003.

[4] G. M. S. AlQahtani, H. M. Alkatan, S. AlMesfer, S. Elkhamary, and A. M. Y. Maktabi, "A case of retinoblastoma masquerading as endophthalmitis: Unusual presentation and clinicopathological correlation," *Int. J. Surg. Case Rep.*, vol. 123, no. September, p. 110263, 2024, doi: 10.1016/j.ijscr.2024.110263.

[5] Y. Liu, Y. Han, S. Chen, J. Liu, D. Wang, and Y. Huang, "Liposome-based multifunctional nanoplatform as effective therapeutics for the treatment of retinoblastoma," *Acta Pharm. Sin. B*, vol. 12, no. 6, pp. 2731–2739, 2022, doi: 10.1016/j.apsb.2021.10.009.

[6] J. Li, A. Li, Y. Liu, L. Yang, and G. Gao, "An adaptive fundus retinal vessel segmentation model capable of adapting to the complex structure of blood vessels," *Biomed. Signal Process. Control*, vol. 101, no. April 2024, 2025, doi: 10.1016/j.bspc.2024.107150.

[7] Y. Xu *et al.*, "Deep learning for predicting circular retinal nerve fiber layer thickness from fundus photographs and diagnosing glaucoma," *Heliyon*, vol. 10, no. 13, p. e33813, 2024, doi: 10.1016/j.heliyon.2024.e33813.

[8] U. A. Nuli, S. D. Desai, and G. N. S. on L. D. P.-S. S. of R. F. I. Bhadri, "Study on Limited Data Problem - Semantic Segmentation of Retinal Fundus Images," *Procedia Comput. Sci.*, vol. 233, pp. 782–792, 2024, doi: 10.1016/j.procs.2024.03.267.

[9] W. Xiao and Y. Lyu, "Human computer interaction product for infrared thermographic fundus retinal vessels image segmentation using U-Net," *J. Radiat. Res. Appl. Sci.*, vol. 17, no. 3, p. 101003, 2024, doi: 10.1016/j.jrras.2024.101003.

[10] W. Huang and F. Liu, "HiDiffSeg: A hierarchical diffusion model for blood vessel segmentation in retinal fundus images," *Expert Syst. Appl.*, vol. 253, no. April, p. 124249, 2024, doi: 10.1016/j.eswa.2024.124249.

[11] T. Fang, Z. Cai, and Y. Fan, "Gabor-net with multi-scale hierarchical fusion of features for fundus retinal blood vessel segmentation," *Biocybern. Biomed. Eng.*, vol. 44, no. 2, pp. 402–413, 2024, doi: 10.1016/j.bbe.2024.05.004.

[12] S. Huang *et al.*, "Automated interpretation of retinal vein occlusion based on fundus fluorescein angiography images using deep learning: A retrospective, multi-center study," *Heliyon*, vol. 10, no. 13, p. e33108, 2024, doi: 10.1016/j.heliyon.2024.e33108.

[13] X. Xia *et al.*, "Benchmarking deep models on retinal fundus disease diagnosis and a large-scale dataset," *Signal Process. Image Commun.*, vol. 127, no. April, p. 117151, 2024, doi: 10.1016/j.image.2024.117151.

[14] C. Y. T. Wong, T. Liu, T. L. Wong, J. M. K. Tong, H. H. W. Lau, and P. A. Keane, "Development and validation of an automated machine learning model for the multi-class

classification of diabetic retinopathy, central retinal vein occlusion and branch retinal vein occlusion based on color fundus photographs," *JFO Open Ophthalmol.*, vol. 7, p. 100117, 2024, doi: 10.1016/j.jfop.2024.100117.

[15] J. Liu *et al.*, "Spectral reconstruction of fundus images using retinex-based semantic spectral separation transformer, applied for retinal oximetry," *Biomed. Signal Process. Control*, vol. 94, no. April, p. 106301, 2024, doi: 10.1016/j.bspc.2024.106301.

[16] S. Balasubramaniam, S. Kadry, and K. Satheesh Kumar, "Osprey Gannet optimization enabled CNN based Transfer learning for optic disc detection and cardiovascular risk prediction using retinal fundus images," *Biomed. Signal Process. Control*, vol. 93, no. February, p. 106177, 2024, doi: 10.1016/j.bspc.2024.106177.

[17] H. J. He, C. Zheng, and D. W. Sun, "Image Segmentation Techniques," *Comput. Vis. Technol. Food Qual. Eval. Second Ed.*, no. December, pp. 45–63, 2016, doi: 10.1016/B978-0-12-802232-0.00002-5.

[18] Z. Liu, X. Jia, and X. Xu, "Study of shrimp recognition methods using smart networks," *Comput. Electron. Agric.*, vol. 165, 2019, doi: 10.1016/j.compag.2019.104926.

[19] D. Li, L. Xu, and H. Liu, "Detection of uneaten fish food pellets in underwater images for aquaculture," *Aquac. Eng.*, vol. 78, no. December 2016, pp. 85–94, 2017, doi: 10.1016/j.aquaeng.2017.05.001.

[20] Y. Han, T. Song, J. Feng, and Y. Xie, "Grayscale-inversion and rotation invariant image description with sorted LBP features," *Signal Process. Image Commun.*, vol. 99, no. June, p. 116491, 2021, doi: 10.1016/j.image.2021.116491.

[21] S. N and V. S, "Image Segmentation By Using Thresholding Techniques For Medical Images," *Comput. Sci. Eng. An Int. J.*, vol. 6, no. 1, pp. 1–13, 2016, doi: 10.5121/cseij.2016.6101.

[22] S. Du, K. Luo, Y. Zhi, H. Situ, and J. Zhang, "Jou lP," *Results Phys.*, p. 105710, 2022, doi: 10.1016/j.rinp.2022.105710.

[23] J. Wang, J. Kosinka, and A. Telea, "Spline-based medial axis transform representation of binary images," *Comput. Graph.*, vol. 98, pp. 165–176, 2021, doi: 10.1016/j.cag.2021.05.012.

[24] N. Halder, D. Roy, P. Roy, and P. Roy, "Qualitative Comparison of OTSU Thresholding with Morphology Based Thresholding for Vessels Segmentation of Retinal Fundus Images of Human Eye," vol. 6, no. 3, pp. 41–48, 2016, doi: 10.9790/4200-0603024148.

[25] X. Hu and Y. Wang, "Catena Monitoring coastline variations in the Pearl River Estuary from 1978 to 2018 by integrating Canny edge detection and Otsu methods using long time series Landsat dataset," *Catena*, vol. 209, no. P2, p. 105840, 2022, doi: 10.1016/j.catena.2021.105840.

[26] R. M. Ambrosi and J. I. W. Watterson, "The effect of the imaging geometry and the impact of neutron scatter on the detection of small features in accelerator-based fast neutron radiography," *Nucl. Instruments Methods Phys. Res. Sect. A Accel. Spectrometers, Detect. Assoc. Equip.*, vol. 524, no. 1–3, pp. 340–354, 2004, doi: 10.1016/j.nima.2003.12.042.

[27] A. K. Jain, *Fundamentals of Digital Image Processing*. Pearson, 1988.

[28] Z. Wu *et al.*, "Effect of nozzle geometry features on the nozzle internal flow and cavitation characteristics based on X-ray dynamic imaging," *Nucl. Instruments Methods Phys. Res. Sect. A Accel. Spectrometers, Detect. Assoc. Equip.*, vol. 1058, no. October 2023, 2024, doi: 10.1016/j.nima.2023.168831.

[29] D. Zeng, T. Zhang, R. Fang, W. Shen, and Q. Tian, "Neighborhood geometry based feature matching for geostationary satellite remote sensing image," *Neurocomputing*, vol. 236, no. March 2016, pp. 65–72, 2017, doi: 10.1016/j.neucom.2016.08.105.

[30] H. Zou, F. Da, and Z. Wang, "A novel 3D face feature based on geometry image vertical shape information," *Optik (Stuttg).*, vol. 126, no. 9–10, pp. 898–902, 2015, doi: 10.1016/j.ijleo.2015.02.083.

[31] M. Bourdeau *et al.*, "Classification of daily electric load profiles of non-residential buildings," *Energy Build.*, vol. 233, p. 110670, 2021, doi: 10.1016/j.enbuild.2020.110670.

[32] P. K. Gandla, V. Inturi, S. Kurra, and S. Radhika, "Evaluation of surface roughness in incremental forming using image processing based methods," *Meas. J. Int. Meas. Confed.*, vol. 164, p. 108055, 2020, doi: 10.1016/j.measurement.2020.108055.

[33] J. P. M. Andries, M. Goodarzi, and Y. Vander Heyden, "Improvement of quantitative structure–retention relationship models for chromatographic retention prediction of peptides applying individual local partial least squares models," *Talanta*, vol. 219, no. June, p. 121266, 2020, doi: 10.1016/j.talanta.2020.121266.

[34] P. Barrett, "Euclidean Distance Whitepaper," *Tech. Whitepaper Ser. 6*, p. 26, 2005.

[35] S. Zhao *et al.*, "Application of machine learning in intelligent fish aquaculture: A review," *Aquaculture*, vol. 540, no. April, p. 736724, 2021, doi: 10.1016/j.aquaculture.2021.736724.

[36] K. Madi, E. Paquet, and H. Kheddouci, "New graph distance for deformable 3D objects recognition based on triangle-stars decomposition," *Pattern Recognit.*, vol. 90, pp. 297–307, 2019, doi: 10.1016/j.patcog.2019.01.040.

[37] K. Swathi and S. Kodukula, "Revue d ' Intelligence Artificielle XGBoost Classifier with Hyperband Optimization for Cancer Prediction Based on Geneselection by Using Machine Learning Techniques," vol. 36, no. 5, pp. 665–670, 2022.

[38] K. Islam, S. Ali, S. Miah, and M. Rahman, "Machine Learning with Applications Brain tumor detection in MR image using superpixels , principal component analysis and template based K-means clustering algorithm," *Mach. Learn. with Appl.*, vol. 5, no. May, p. 100044, 2021, doi: 10.1016/j.mlwa.2021.100044.

[39] D. Mou, Z. Wang, X. Tan, and S. Shi, "A variational inequality approach with SVM optimization algorithm for identifying mineral lithology," *J. Appl. Geophys.*, vol. 204, no. December 2021, p. 104747, 2022, doi: 10.1016/j.jappgeo.2022.104747.

[40] M. Mustaqeem, "Principal component based support vector machine (PC-SVM): a hybrid technique for software defect detection," *Cluster Comput.*, vol. 24, no. 3, pp. 2581–2595, 2021, doi: 10.1007/s10586-021-03282-8.

[41] Y. Wang *et al.*, "Abnormal intrinsic brain functional network dynamics in patients with retinal detachment based on graph theory and machine learning," *Heliyon*, vol. 10, no. 23, 2024, doi: 10.1016/j.heliyon.2024.e37890.

[42] M. Saberioon and P. Císař, "Automated within tank fish mass estimation using infrared reflection system," *Comput. Electron. Agric.*, vol. 150, no. May, pp. 484–492, 2018, doi: 10.1016/j.compag.2018.05.025.

[43] V. C. F. Aiken, J. R. R. Dórea, J. S. Acedo, F. G. de Sousa, F. G. Dias, and G. J. de M. Rosa, "Record linkage for farm-level data analytics: Comparison of deterministic, stochastic and machine learning methods," *Comput. Electron. Agric.*, vol. 163, no. March, p. 104857, 2019, doi: 10.1016/j.compag.2019.104857.

[44] W. Gao and Z. H. Zhou, "Towards convergence rate analysis of random forests for classification," *Adv. Neural Inf. Process. Syst.*, vol. 2020-Decem, p. 103788, 2020, doi: 10.1016/j.artint.2022.103788.

[45] G. Yoshikazu, P. Krecl, and A. Créso, "Science of the Total Environment Fine-scale modeling of the urban heat island : A comparison of multiple linear regression and random forest approaches," vol. 815, 2022, doi: 10.1016/j.scitotenv.2021.152836.

[46] A. Zermane, M. Z. Mohd Tohir, H. Zermane, M. R. Baharudin, and H. Mohamed Yusoff, "Predicting fatal fall from heights accidents using random forest classification machine learning model," *Saf. Sci.*, vol. 159, no. November 2022, p. 106023, 2023, doi: 10.1016/j.ssci.2022.106023.

[47] M. Ghane, M. C. Ang, M. Nilashi, and S. Sorooshian, "Enhanced decision tree induction using evolutionary techniques for Parkinson's disease classification," *Biocybern. Biomed. Eng.*, vol. 42, no. 3, pp. 902–920, 2022, doi: 10.1016/j.bbe.2022.07.002.

[48] L. Spirkovska, "Three-dimensional object recognition using similar triangles and decision trees," *Pattern Recognit.*, vol. 26, no. 5, pp. 727–732, 1993, doi: 10.1016/0031-3203(93)90125-G.

[49] S. K. Singla, R. D. Garg, and O. P. Dubey, "Ensemble machine learning methods to estimate the sugarcane yield based on remote sensing information," *Rev. d'Intelligence Artif.*, vol. 34, no. 6, pp. 731–743, 2020, doi: 10.18280/RIA.340607.

[50] A. K. Al-Musawi, F. Anayi, and M. Packianather, "Three-

phase induction motor fault detection based on thermal image segmentation," *Infrared Phys. Technol.*, vol. 104, no. November 2019, p. 103140, 2020, doi: 10.1016/j.infrared.2019.103140.

[51] G. M. H. Amer and A. M. Abushaala, "Edge detection methods," *2015 2nd World Symp. Web Appl. Networking, WSWAN 2015*, no. August 2015, pp. 1–8, 2015, doi: 10.1109/WSWAN.2015.7210349.

[52] C. E. Widodo and K. Adi, "Face geometry as a biometric-based identification system," *J. Phys. Conf. Ser.*, vol. 1524, no. 1, 2020, doi: 10.1088/1742-6596/1524/1/012008.

[53] Y. Yang, X. Zhao, M. Huang, X. Wang, and Q. Zhu, "Multispectral image based germination detection of potato by using supervised multiple threshold segmentation model and Canny edge detector," *Comput. Electron. Agric.*, vol. 182, no. September 2020, p. 106041, 2021, doi: 10.1016/j.compag.2021.106041.